Relationship Between Rupture Length and Magnitude of Oceanic Transform Fault Earthquakes

Guilherme W. S. de Melo[1] ⓘ**, Ingo Grevemeyer[1]** ⓘ**, Dietrich Lange[1]** ⓘ**, Dirk Metz[2], and Heidrun Kopp[1]** ⓘ

[1]GEOMAR Helmholtz Centre of Ocean Research Kiel, Kiel, Germany, [2]Preparatory Commission for the Comprehensive Nuclear-Test-Ban Treaty Organization (CTBTO), Vienna, Austria

Abstract The rupture behavior of large oceanic strike-slip earthquakes remains largely unresolved using seismic signals recorded thousands of kilometers away from the source area. Large submarine earthquakes, however, generate hydroacoustic T-waves propagating through the ocean over long distances. Here, we show that these T-waves recorded at regional distances on the Ascension hydrophone array of the International Monitoring System can provide critical information on the earthquake location and rupture behavior. We use recordings from 47 events in oceanic transform faults, ranging in magnitude from $5.6 \leq M_w \leq 7.1$, to investigate the rupture processes. We find that most strike-slip earthquakes show unilateral rupture behavior, while a few larger events were more complex. Furthermore, earthquakes in oceanic transforms have longer ruptures than events of the same magnitude in continental faults. We argue that differences in the scaling relation of oceanic and continental strike-slip earthquakes support a lower rigidity in the oceanic lithosphere caused by hydration.

Plain Language Summary Oceanic transform faults are strike-slip faults where one plate moves past another laterally, with new seafloor created at adjacent mid-ocean ridge segments on either side of the transform. At the transforms, plate motion generates strong earthquakes, causing seismic waves to propagate for thousands of kilometers. Nevertheless, due to their remoteness the rupture behavior of oceanic earthquakes and their scaling relationship between magnitude and rupture length is poorly constrained and understood. Here, we use hydroacoustic signals, so-called T-waves, which are excited by seismic deformation of the seafloor. T-waves are readily observable at the International Monitoring System hydrophone triplet near Ascension Island, Atlantic Ocean. We present a new relationship between the magnitude of equatorial Atlantic strike-slip earthquakes and the rupture length from 47 events (M_W 5.6–7.1). We found that oceanic earthquakes differ from continental ones, showing longer ruptures for the same magnitude, suggesting that oceanic transform faults are weak.

1. Introduction

Earthquake magnitude and rupture parameters (e.g., rupture length, velocity or direction) are inherently related and provide critical information about seismic hazards and the physics of faulting. Relationships between the size of a rupture (e.g., length or width) and the magnitude are reasonably well-known for earthquakes in continental settings or close to continents, including subduction zones (e.g., Blaser et al., 2010; Wells & Coppersmith, 1994), but are poorly resolved for oceanic transform faults (OTF) located thousands of kilometers away from seismic land stations. Furthermore, continental fault zones are dominated by rocks characterized by a rheology controlled by quartz and plastic deformation at temperatures >450°C (e.g., Scholz, 1988), while faulting in the oceanic lithosphere is related to olivine minerals and a brittle-to-ductile transition occurring at ~600°C (Searle & Escartin, 2013). The relation of rheology to rupture behavior and scaling relationships is poorly known.

Rupture length and width are generally constrained from aftershocks, geodetic estimates, finite source models, and back-projection (e.g., Goldberg et al., 2022; Mai & Beroza, 2000; Vera et al., 2024; Wells & Coppersmith, 1994). Unfortunately, only a small number of aftershocks are commonly recorded for large strike-slip earthquakes rupturing along OTFs (Boettcher & Jordan, 2004; McGuire et al., 1996), and finite source models without geodetic constraints might be poorly resolved (Goldberg et al., 2022). However, oceanic earthquakes cause energy coupling into the ocean forming several minutes and up to tens of minutes long wavetrains, called Tertiary or T-waves (e.g., Okal, 2008; I. Tolstoy and Ewing, 1950). T-waves are hydroacoustic waves that propagate over long distances through the ocean as guided waves (e.g., Okal, 2008) trapped in the SOFAR

Resources: Guilherme W. S. de Melo, Ingo Grevemeyer
Software: Guilherme W. S. de Melo
Supervision: Ingo Grevemeyer, Heidrun Kopp
Validation: Guilherme W. S. de Melo, Ingo Grevemeyer, Dirk Metz
Writing – original draft: Guilherme W. S. de Melo
Writing – review & editing: Guilherme W. S. de Melo, Ingo Grevemeyer, Dietrich Lange, Dirk Metz, Heidrun Kopp
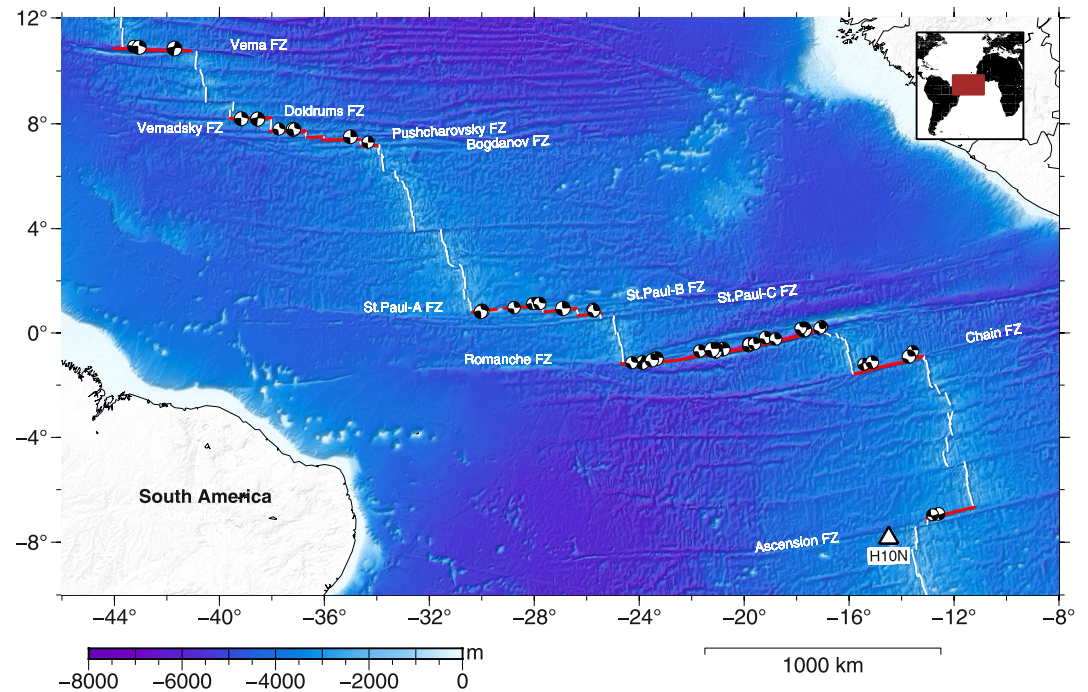
Figure 1. Bathymetric map of the equatorial Atlantic together with 47 strike-slip earthquakes along transform faults from the Global Centroid Moment Tensor (GCMT) catalog. White triangle represents the location of the H10N hydrophone triplet deployed ∼20 km north of Ascension Island. Red traces indicate the oceanic transforms studied, with the mapped mid-ocean ridges presented in white traces from the MAPRIDGES database (Sautter et al., 2024).

(Sounding Fixing and Ranging) channel to be recorded at seismometers or hydrophones in the ocean, often thousands of kilometers away.

T-waves are widely used to locate small mid-ocean ridge (MOR) earthquakes using temporary and widely spaced hydrophones moored in the SOFAR channel (R. P. Dziak and Fox, 1999; Ingale et al., 2023; Parnell-Turner et al., 2022; Smith et al., 2003). Hydroacoustic signals were also used to constrain the oceanic uppermost mantle structure (de Melo et al., 2021; Dziak et al., 2004). In addition, it was shown that T-waves can be used to reveal rupture propagation of large earthquakes, like the 2004 $M_W = 9.3$ Sumatra earthquake, with a fault rupture of ∼1,200 km along the Sumatra subduction zone (de Groot-Hedlin, 2005; Guilbert et al., 2005; M. Tolstoy and Bohnenstiehl, 2005). These studies used hydrophone arrays of the International Monitoring System (IMS) deployed by the Comprehensive Nuclear-Test-Ban Treaty Organization (CTBTO) to detect possible nuclear tests (Gibbons, 2022) and showed that hydroacoustic records lead to similar results presented by seismological records in assessing the rupture behavior of submarine earthquakes (P. Shearer and Bürgmann, 2010). Here, we use T-waves registered on a hydrophone array offshore Ascension Island in the equatorial Atlantic to investigate the rupture parameters of oceanic strike-slip earthquakes reported by the Global Centroid Moment Tensor (GCMT) project (Dziewonski et al., 1981; Ekström et al., 2012).

We study earthquakes occurring along OTFs in the equatorial Atlantic, offsetting the Mid-Atlantic Ridge by tens to hundreds of kilometers (Maia, 2019; Wilson, 1965). The longest OTF in our study is the ∼840 km long Romanche (Ren et al., 2022; Searle et al., 1994) and the shortest are the 40–80 km long Bogdanov and St. Paul-C OTF (Wolfson-Schwehr & Boettcher, 2019). The Atlantic OTFs are seismically active with earthquakes of magnitude reaching >7.0 (Frohlich & Wetzel, 2007). We use our estimates of rupture length and seismic moment to investigate a unique scaling relationship of oceanic strike-slip earthquakes.

2. Methodology

2.1. Ascension Hydroacoustic Data

In 2004, the H10N hydrophone array was installed to the north of Ascension Island as part of the IMS (Figure 1). H10N consists of three hydrophones (H10N1, H10N2, and H10N3, http://www.fdsn.org/networks/detail/IM/) that are deployed approximately 850 m below sea level with an array aperture of 2 km. The signals are recorded with a sampling rate of 250 Hz and transmitted in real-time to the International Data Center. For the time period from January 2015 onward, data from H10N are available via EarthScope (e.g., Gibbons, 2022), offering a rich database of T-waves generated by submarine earthquakes from the Atlantic Ocean.

Since 2015, 53 strike-slip earthquakes related to OTFs from the North Atlantic are listed in the GCMT catalog with Mw between 5.6 and 7.1 and source-receiver distances ranging from 208 to 3,803 km. We only investigate earthquakes where both hydrophone data and multibeam bathymetric data are available. Our catalog lists 47 strike-slip earthquakes from 11 OTFs (Figure 1), providing robust back azimuth estimates and includes 7 events from before 2015 used to implement data analyses.

2.2. Source Direction, Rupture Area, and Uncertainties Calculation

Seismic energy radiated by an oceanic earthquake excites hydroacoustic T-waves over the focal area. The arrival times of the energy approaching the hydrophones are used to estimate the direction of the earthquake source (Del Pezzo & Giudicepietro, 2002). We applied a 2–4 Hz bandpass filter to reduce low and high-frequency noise contamination. The time differences between the three hydrophones produce three peak delays calculated by cross-correlating the three signal pairs ($t_{ij} + t_{jk} + t_{ki}$) to each time window of 40 s with a 25% overlap. The sum of the time delay between the three hydrophone pairs is assumed to approach zero for perfectly correlated signals and is expressed by the closure function (Bohnenstiehl et al., 2002):

$$cl = (t_{ij} + t_{jk} + t_{ki}) \tag{1}$$

Following the approach from M. Tolstoy and Bohnenstiehl (2005), we estimate the arrival of the T-wave at the array using the GCMT origin time and a T-velocity model of the Global Ocean Sound Speed Profile Library (Barlow, 2019). Appropriate T-wave velocities are constant for each event and range from 1.46 km/s to 1.57 km/s (Figures S1-S8 in Supporting Information S1). The onset and end time of the final analysis window was defined as the position where the spectral energy is high (Figures 2a and 2b), and the mean of the three cross-correlation coefficients tends to be closest to 1 (Figure 2c). The location difference between each pair of stations $\Delta x_{ij} = (x_i - x_j, y_i - y_j)$, where x_i, y_i refers to the distance between the two instruments in a Cartesian plane (Del Pezzo & Giudicepietro, 2002). Following the 2D plane wave fitting approach, we calculate the back azimuth of the incoming signal using the slowness vector $p = (p_x, p_y)$ and solving a least-square approach $p = (\Delta x^T \Delta x)^{-1} \Delta x^T t$ (Del Pezzo & Giudicepietro, 2002). Given that, the slowness vector is obtained and then the apparent velocity (v) and back azimuth (θ) direction (Figure 2d) of the T-wave source are calculated by

$$v = \left(p_x^2 + p_y^2\right)^{-\frac{1}{2}} \tag{2}$$

$$\theta = tan^{-1}\left(\frac{p_x}{p_y}\right) \tag{3}$$

The absolute errors for both back azimuth and apparent velocity are estimated using the covariance matrix of the inversion and a 95% confidence interval for each time window, assuming a normal distribution (Metz et al., 2018).

Recordings from the hydrophone triplet provide high-accuracy back-azimuths for seismo-acoustic sources located close to or within the SOFAR channel, such as erupting submarine volcanoes (e.g., Metz et al., 2016). However, submarine earthquakes occur within the seafloor well below the SOFAR channel and thus energy needs to couple into it (Okal 2008; Talandier & Okal, 1998). We therefore explore the accuracy of T-wave derived back-azimuths by comparing the average back azimuth to epicenter locations from global catalogs and studying the distance between two T-wave epicenters and the corresponding distance derived from cross-correlation of surface waves. Observations derived from T-wave energy and seismological centroids compare well (Text S1, Figures S9
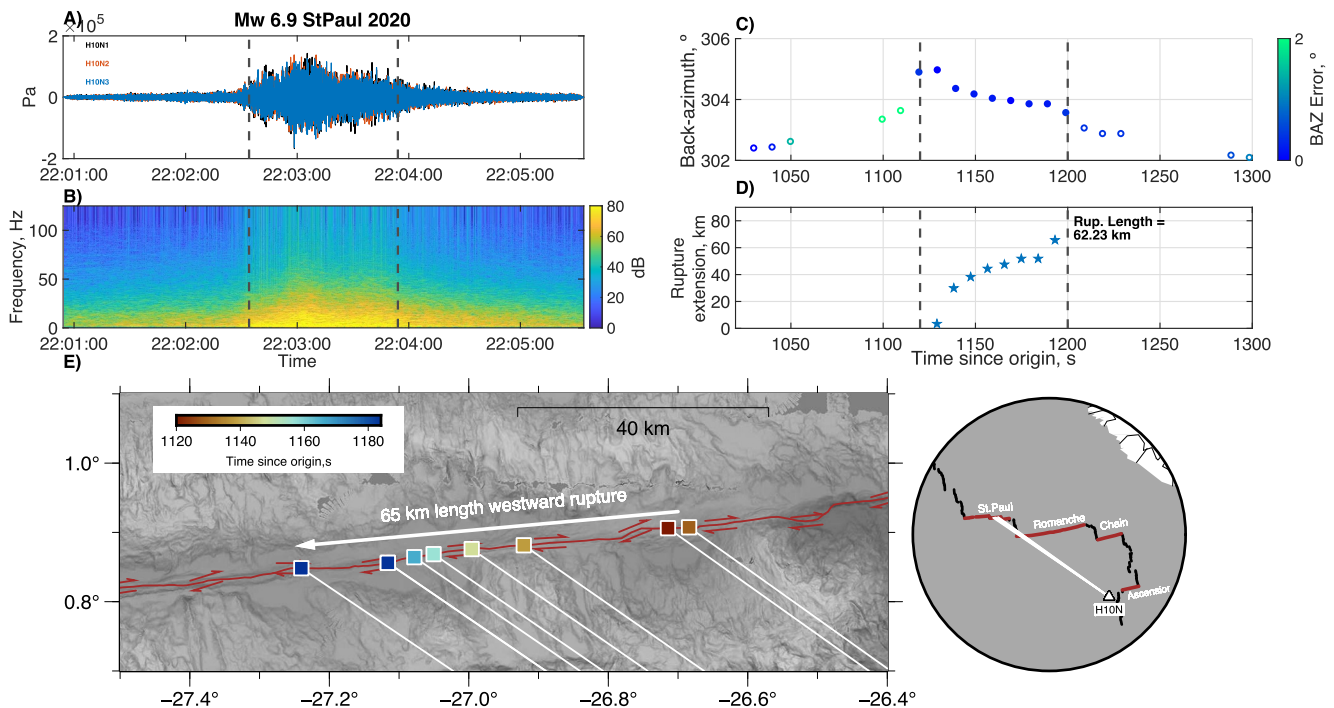
Figure 2. Hydroacoustic T-wave of the 2020 M_W 6.9 St. Paul earthquake recorded at the H10N hydrophone array. (a) Shows the T waveforms of the three hydrophones with a 2 Hz high-pass filter used to remove the lower frequency noise. Dotted lines indicate the start and end points of the analyzed waveform. They were selected from the higher energy observed from the spectrogram of the H10N1 hydrophone shown in (b). (c) Back-azimuths obtained from cross-correlation of three-hydrophone pairs; unfilled circles mark measurements not used as the cross-correlation/closure was poor. In (d), stars indicate the cumulative horizontal rupture extent after projection of the back azimuths onto the bathymetry. Time relates to the origin time of the earthquake. (e) Map with zoom-in in rupture area. Squares refer to the interceptions of the back-azimuths (white lines) with the active fault; color presents the time of rupture propagation. The rupture direction is shown by the white arrow.

and S10a in Supporting Informartion S1), suggesting that T-wave estimates provide robust constraints on the rupture of submarine earthquakes.

The estimation of the back azimuth of the T-wave source is done in three steps (Figures S1–S10 in Supporting Information S1): first, we use the multibeam data of each transform fault to trace the fault along the transform valley. Then, we projected the back-azimuths from the mean position of the hydrophone array to the mapped fault trace. Lastly, the path where each back-azimuth intercepts the fault is marked as the T-wave excitation position (de Groot-Hedlin, 2005; M. Tolstoy and Bohnenstiehl, 2005). The cumulative rupture length is calculated from the sum of the distances between two adjacent excitation points. The surface rupture length (RL) is derived from the distance between the most eastward and westward geographical position of back-projected T-wave energy (Figure 2e), including the associated uncertainty (details of RL uncertainty are discussed in the Supporting Information S1; Text S1 in Supporting Information S1). We assume that the horizontal length of the rupture is greater than the vertical. Then, the seismic rupture velocity (see figures on Supporting Information S1; https://doi.org/10.5281/zenodo.12580246) was approximated using the horizontal distance and the time variation between each back-azimuth pair (Guilbert et al., 2005).

3. Results

We provide unique hydroacoustic estimates on the rupture characteristics of 47 earthquakes from 11 OTFs (Table S1 in Supporting Information S1), showing a clear relationship between the acoustic magnitude called source level (SL) and M_W (Text S2 and Table S4 in Supporting Information S1), SL versus epicentral distance (Figure S7 in Supporting Information S1), and RL increasing with increasing moment magnitude M_W (Figure 3). In general, we estimate RL ranging from 4 ± 1 to 81 ± 8 km for earthquakes of $5.6 \leq M_W \leq 7.1$ (Table S1 in Supporting Information S1). Earthquakes smaller than $M_W = 6$ have ruptures with lengths shorter than 20 km and a roughly linear scaling relationship between RL and M_W. In addition, all $M_W < 6$ earthquakes show unilateral rupture. In total, 43 events reveal unilateral wavefront propagation and only four earthquakes of $M_W \geq 6.1$ show a more
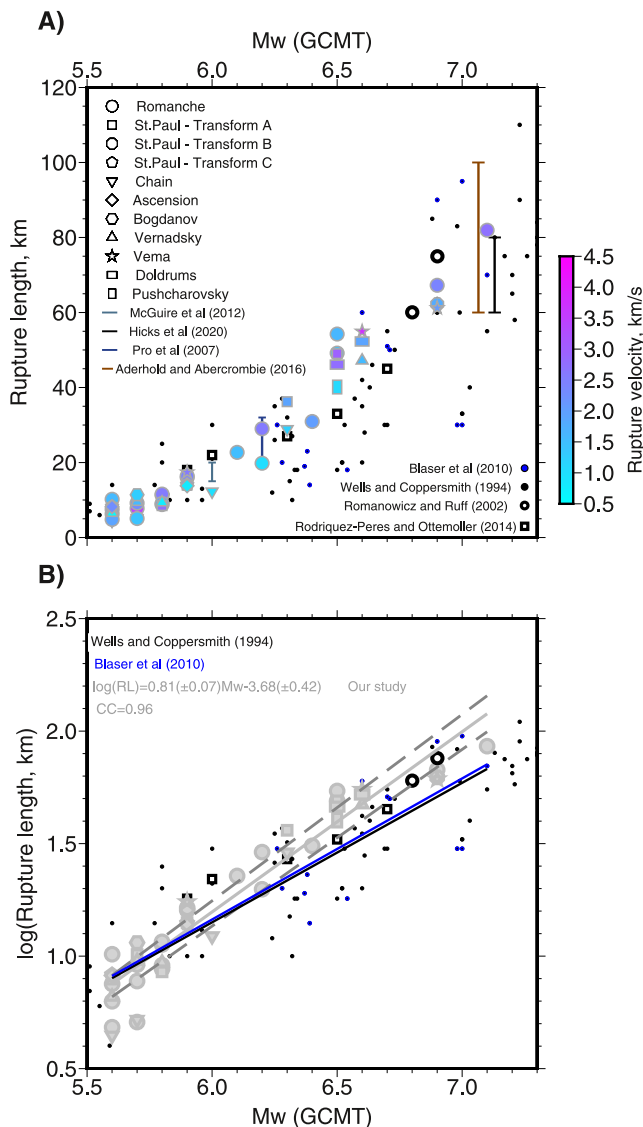
Figure 3. (a) Relationship of moment magnitude (M_W) and rupture length (RL) from T-waves (symbols), rupture velocity is color-coded. Black and blue points refer to strike-slip earthquakes from Wells and Coppersmith (1994) and Blaser et al. (2010), respectively. Open black circles: the 1967 M_S 6.7 and 1974 M_S 6.9 Charlie-Gibbs earthquakes (Romanowicz & Ruff, 2002); brown and black vertical lines: the 2015 M_W 7.1 Charlie-Gibbs (Aderhold & Abercrombie, 2016) and the 2016 M_W 7.1 Romanche (Hicks et al. 0) earthquakes; skyeblue line: the 2007 M_W 6.0 Gofar (McGuire et al., 2012) earthquake, royalblue: 2003 Mw 6.2 Oceanographer earthquake (Pro et al., 2007), open black squares: five Mw = 5.9–6.7 Jan Mayen transform earthquakes (Rodríguez-Péres and Ottemöller 2014). (b) Same as (a) but log (RL), symbols with dark gray outline refer to the OTFs in (a). Gray lines show least squares regression obtained from our RL estimates; darkgray dashed lines represent the 95% confidence.

complex rupture behavior. Earthquakes of M_W 6.0 to 7.1 yield a much larger variability in RL for the same magnitude; for example, for $M_W = 6.5$ RL varies from ~35–60 km (Figure 3).

The Romanche transform (1.2°S–0.2°N) at the equator provides with 21 earthquakes the largest number of events. Magnitudes range from M_W 5.6–7.1 and RL varies from 5 ± 2 km to 81 ± 8 km. The largest event, the 2016 M_W 7.1 earthquake (Hicks et al., 2020), is one of the few events showing more complex rupture patterns propagating in two phases (or two-steps), reversing its rupture direction over time. The shorter OTFs of <100 km offset do not show any earthquake of $M_W > 6$, while longer OTFs generally show strong events of $M_W \geq 6.2$, like the Doldrums transform (8.2°N), revealing a $M_W = 6.5$ and 6.6 with ruptures of 46 ± 6 km and 63 ± 3 km, respectively; the St. Paul system shows RL ranging from 8 ± 4 to 62 ± 6 km (5.6 ≤ Mw ≤ 6.9). The Vema OTF, the most distant fault studied, provides three events of 5.9–6.9 with RL ranging from 20 ± 3 km to 61 ± 6 km, including a $M_W = 6.6$ showing a two-step rupture. Most importantly, our estimates show a unique scaling relationship between M_W and RL (Figure 3) for submarine strike-slip earthquakes.

The average rupture velocity derived from T-wave back-azimuths ranges for events with small relative RL uncertainty from 1.02 to 4.76 km/s. The fastest rupture was observed for the Romanche OTF and the slowest for the Chain OTF. The maximum velocity of 5.85 km/s was identified for the 2016 M_W 7.1 Romanche earthquake, showing supershear rupture (Bao et al., 2022; Hicks et al., 2020). The T-wave derived rupture velocities do not correlate with neither RL nor M_W, but the slowest velocities are associated with earthquakes of $M_W < 5.8$.

4. Discussion and Conclusions

4.1. Rupture Behavior From Hydroacoustic Versus Seismological Observations

Much of our understanding of earthquake processes in remote oceanic settings is derived from global seismic catalogs, but T-waves contribute to characterize sub-marine earthquakes. Distance-corrected SL of T-wave energy, the hydroacoustic equivalent to magnitude, scales well with the M_W from the GCMT catalog (Figure S11 in Supporting Information S1), and RL scales both with M_W (Figure 3a) and the length of the SCARDEC (Vallee & Douet, 2016; http://scardec.projects.sismo.ipgp.fr/) source time function of earthquakes (Figure S12 in Supporting Information S1). In addition, the total T-wave duration scales well with the RL and SCARDEC source time (Figure S13 in Supporting Information S1), but it is well known that all sub-marine earthquakes cause T-waves of long duration (e.g., Okal & Talandier, 1986). Simulations of T-waves suggest that those long wavetrains are related to scattering of energy at rough seafloor caused by converted P-waves in the water column with multiple reverberations (Groot-Hedlin and Orcutt, 1999; Jamet et al., 2013; Talandier & Okal, 1998; Yang & Forsyth, 2003), and by the T-wave propagation (Chen et al., 2017; Jamet et al., 2013). Thus, temporal variations of rupture along a fault are obscured by processes of exciting hydroacoustic waves. Therefore, T-wave arrivals are not directly related to

the rupture duration, but still provide accurate measures of back-azimuth and hence the horizontal extension of the source region (e.g., Guilbert et al., 2005; M. Tolstoy and Bohnenstiehl 2005) as was found by P. Shearer and Bürgmann (2010) when comparing results from seismic and hydroacoustic constraints on the source area of the 2004 Sumatra earthquake.
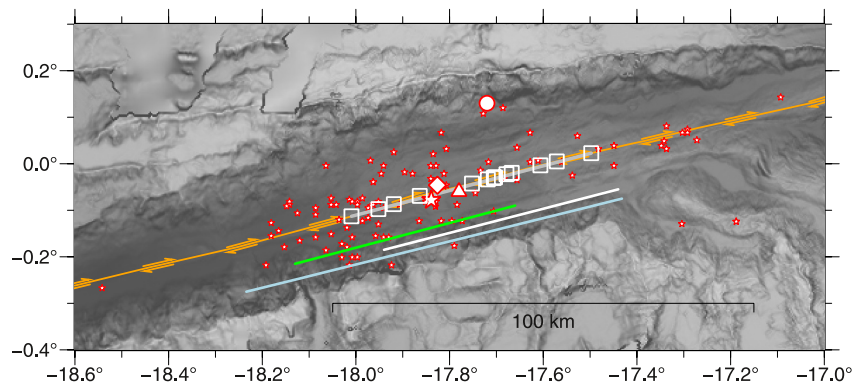
Figure 4. Multibeam bathymetric map showing the rupture for the 2016 M_w 7.1 Romanche earthquake. Red diamond, triangle, circle and star show the epicenter locations of the USGS, GEOFON, GCMT, and Hicks et al. (2020), respectively. Gray line shows the longitudinal ruptured extent obtained by back-azimuths (white squares). Green and white lines show the rupture extent from back-projections (Bao et al., 2022; Hicks et al., 2020). The extent of the earthquake ruptures obtained by finite faults models of the USGS is presented by the light blue line. Aftershock seismicity is shown by red stars (Hicks et al., 2020).

RLs for OTF earthquakes are poorly known due to their low aftershock productivity reported in global catalogs (Boettcher & Jordan, 2004; McGuire et al., 1996). McGuire et al. (1996) studied the 1994 M_W 7.0 Romanche earthquake and suggested that its rupture extended 50–70 km along the transform, but based this assessment on scaling relations. Hicks et al. (2020) recorded aftershocks of the 2016 M_W 7.1 Romanche earthquake at a regional seismic network of ocean-bottom-seismometers (OBS), revealing that aftershocks extended for ∼110 km along the fault (Figure 4). Both Hicks et al. (2020) and Bao et al. (2022) used back-projection analysis and found that the rupture of the same earthquake extended 60–80 km along strike, revealing a complex source process changing direction and showing an episode of supershear rupture. In addition, the finite fault model of the USGS indicated an RL of 70–80 km (Text S3, Figure S14 in Supporting Information S1). Our estimates result in an RL of 81 km and hence provide a similar RL as derived from established seismological methodologies (Figure 4). However, the slightly larger aftershock zone may suggest that static or dynamic stress changes also triggered seismic activity adjacent to the co-seismic fault segment (e.g., de Melo, Mitchell, & Sokolov, 2024). For the Oceanographer OTF, Pro et al. (2007) estimated for a Mw = 6.2 a RL of 21–32 km. At the Gofar OTF, a non-Atlantic OTF located in Pacific Ocean, McGuire et al. (2012) obtained for a Mw = 6.0 event an RL range of 15–20 km based on the aftershock distribution recorded by a local network of OBS. These seismological results match our scaling relationship and hence suggest that T-wave estimates for RL are robust within the uncertainties.

4.2. Global Scaling Relationships

Scaling relationships between M_W and RL of strike-slip earthquakes are of ample importance to understand the physics of earthquakes, yet are only available for continental earthquakes. M_W is routinely reported, for example, in the GCMT project for submarine earthquakes of M_W > 4.8. The length and width of a rupture area are more difficult to assess and are generally derived using finite-fault source modeling (e.g., Mai & Beroza, 2000) or the spatial pattern of aftershocks (Blaser et al., 2010; Konstantinou et al., 2005; Wells & Coppersmith, 1994). Blaser et al. (2010) found no difference in the relationships between Mw and RL of oceanic and continental strike-slip earthquakes, but all events classified as oceanic occurred in submerged continental crusts and not in oceanic lithosphere. In contrast to all previous studies, we studied solely earthquakes in the oceanic lithosphere.

We find a RL versus M_W relationship for oceanic strike-slip events and obtain an excellent fit with a correlation coefficient of 0.97 (Figures 3a and 3b). We find that RL estimates increase with M_W and agree well with the few available constraints on RL and magnitude for the Oceanographer (Pro et al., 2007), Jan Mayen (Rodríguez-Pérez & Ottemöller, 2014), Charlie-Gibbs (Aderhold & Abercrombie, 2016; Kanamori & Stewart, 1976) and Romanche OTF (Bao et al., 2022; Hicks et al., 2020). Interestingly, our empirical correlation yields longer ruptures for a given magnitude than obtained by Wells and Coppersmith (1994) and Blaser et al. (2010) (see black and blue lines in Figure 3b) for continental earthquakes with equal M_W. Rodríguez-Pérez and Ottemöller (2014) found that their oceanic RLs for the Jan Mayen OTF are also larger than that predicted by the Wells and

Coppersmith (1994) relationship. One explanation might be that differences in the quartz-dominated continental versus the olivine-dominated oceanic rheology control the scaling relationship. For example, in the continental lithosphere, plastic deformation occurs above ∼450°C (Scholz, 1988), while in the oceanic lithosphere, brittle earthquake rupture occurs at <600–900°C (Prigent et al., 2020; Searle & Escartin, 2013).

Kanamori (1977) defined that the moment release of earthquakes can be characterized by M_W (Text S4 in Supporting Information S1), being $M_W = 2/3log_{10}M_0 - 10.7$, where M_0 refers to the seismic moment ($M_0 = \mu AD$). M_0 depends on the rigidity (μ), the rupture area (A), and displacement (D). The rupture area is the product of RL and the width W (depth of seismic faulting). Therefore, to have a longer RL for a given M_0 the product of μ W D must be smaller for oceanic earthquakes.

Let us consider first W. Along continental fault zones, most earthquakes occur in the crust at <20 km depth, reaching only in collision zones larger depth (Maggi et al., 2000). At continental transform faults, seismicity is restricted to the upper and middle crust. For example, along the San Andreas Fault, seismic activity is confined to a depth of 12–20 km (Ross et al., 2019; Smith-Konter et al., 2011) in a crustal thickness of 32–34 km (Yang et al., 2022). Along the Anatolian Fault Zone, the seismogenic zone extends down to ∼18 km depth (Barbot et al., 2023) in a crustal thickness of 30–32 km (Ogden & Bastow, 2022). In contrast, oceanic crust is generally 4–8 km thick (e.g., Y. J. Chen 1992; Grevemeyer et al., 2018), and hence earthquakes at OTFs frequently reach into the upper mantle, showing centroids at 8–20 km depth (Abercrombie & Ekstrom, 2001; Fang & Abercrombie, 2023; Grevemeyer, 2020). Within the uncertainty of estimates, both continental and oceanic earthquakes support a similar depth range for the maximum depth of rupture, suggesting that the larger RL is not compensated by a smaller width of the fault; hence, it is the product of μ D that must be smaller for oceanic than continental earthquakes.

OTFs show a large slip deficit (Brune, 1968) with 75% of worldwide plate motion along OTFs being accommodated aseismically (e.g., Boettcher & Jordan, 2004). Froment et al. (2014) suggest that the deficit results from segmenting the fault with either domains of intact oceanic crust and mantle or domains of low-velocities that cannot store the strain energy required to nucleate large earthquakes. At the Romanche, low-velocities characterize the transform valley, reaching deep into the mantle (Gregory et al., 2021). Rigidity itself can be calculated from the product of density and the square of the shear wave velocity (e.g., P. M. Shearer 2019). Therefore, domains of profoundly reduced seismic velocity may support a significantly reduced rigidity (Sallares & Ranero, 2019). At OTFs, such domains are suggested to be characterized by strongly hydrated crust or mantle (Kohli et al., 2021; Leptokaropoulos et al., 2023). For example, at the St. Paul OTF, serpentinized peridotite is abundant along the Atoba Ridge (Bickert et al., 2023; Maia et al., 2016). Furthermore, the strength of the oceanic lithosphere can change quickly in hydrated mantle (e.g., Escartin et al., 2001). We therefore, hypothesize that hydration lowers the rigidity of OTFs to values much lower than found along continental fault zones (Text S4 in Supporting Information S1) and argue that the reduction of μ dominates the product of μ D and therefore conclude that earthquakes of the same magnitude provide longer ruptures in oceanic than continental transform faults.

Data Availability Statement

The H10N array data was downloaded from EarthScope Consortium Inc (https://service.iris.edu/), including the following network: (1) The IM (International Miscellaneous Stations, International Federation of Digital Seismograph Networks; Various Institutions, 1965). Hydroacoustic data for seven events from before January 2015 were made available by the CTBTO International Data Centre, Vienna, through the virtual Data Exploitation Centre (vDEC, www.ctbto.org/specials/vdec/). For the data analyzes and processing we used MATLAB version 9.8 (The MathWorks Inc, 2020) with toolboxes (Control System; Signal Processing; Mapping; Antenna; Communications; Phased Array System; The MathWorks Inc, 2020) and other external codes obtained in MathWorks File Exchange (e.g., DEG2UTM; Palacios, 2024; GRDREAD2; Jordahl, 2024; RDSAC; Beauducel, 2024). Additional Supporting Information S1 for all earthquakes is accessible using the Zenodo repository (de Melo, Grevemeyer, et al., 2024). The Generic Mapping Tools, version 6 (Wessel et al., 2019), were used to produce maps and graphics. Other figures were created using MATLAB version 9.8. Bathymetric data used for the Ascension and Vema transforms are available at Ren et al. (2021). Figure 1 uses bathymetry downloaded from the Global Multi-Resolution Topography (https://www.gmrt.org/GMRTMapTool; Ryan et al., 2009) and the segmentation of the Mid-Atlantic Ridge is from Sautter et al. (2024).

Disclaimer

The views expressed in this study are those of the authors and do not necessarily reflect those of the Preparatory Commission for the CTBTO.

References

Abercrombie, R. E., & Ekstrom, G. (2001). Earthquake slip on oceanic transform faults. *Nature*, *410*(6824), 74–77. https://doi.org/10.1038/35065064

Aderhold, K., & Abercrombie, R. E. (2016). The 2015 Mw 7.1 earthquake on the Charlie-Gibbs transform fault: Repeating earthquakes and multimodal slip on a slow oceanic transform. *Geophysical Research Letters*, *43*(12), 6119–6128. https://doi.org/10.1002/2016GL068802

Bao, H., Xu, L., Meng, L., Ampuero, J.-P., Gao, L., & Zhang, H. (2022). Global frequency of oceanic and continental supershear earthquakes. *Nature Geoscience*, *15*(11), 942–949. https://doi.org/10.1038/s41561-022-01055-5

Barbot, S., Luo, H., Wang, T., Hamiel, Y., Piatibratova, O., Javed, M. T., et al. (2023). Slip distribution of the February 6, 2023 Mw 7.8 and Mw 7.6, Kahramanmaras, Turkey earthquake sequence in the east Anatolian fault zone. *Seismica*, *2*(3). https://doi.org/10.26443/seismica.v2i3.502

Barlow, J. (2019). *Global ocean sound speed profile library (GOSSPL), an data resource for studies of ocean sound propagation* (Vol. 612). NOAA Technical Memorandum NMFS SWFSC. https://doi.org/10.25923/7dj1-j540

Beauducel, F. (2024). RDSAC and MKSAC: Read and write SAC seismic data file. *GitHub*. https://github.com/IPGP/sac-lib

Bickert, M., Kaczmarek, M.-A., Brunelli, D., Maia, M., Campos, T. F., & Sichel, S. E. (2023). Fluid-assisted grain size reduction leads to strain localization in oceanic transform faults. *Nature Communications*, *14*(1), 4087. https://doi.org/10.1038/s41467-023-39556-5

Blaser, L., Kruger, F., Ohrnberger, M., & Scherbaum, F. (2010). Scaling relations of earthquake source parameter estimates with special focus on subduction environment. *Bulletin of the Seismological Society of America*, *100*(6), 2914–2926. https://doi.org/10.1785/0120100111

Boettcher, M. S., & Jordan, T. (2004). Earthquake scaling relations for mid-ocean ridge transform faults. *Journal of Geophysical Research*, *109*(B12). https://doi.org/10.1029/2004JB003110

Bohnenstiehl, D., Tolstoy, M., Dziak, R., Fox, C., & Smith, D. (2002). Aftershock sequences in the mid-ocean ridge environment: An analysis using hydro acoustic data. *Tectonophysics*, *354*(1–2), 49–70. https://doi.org/10.1016/S0040-1951(02)00289-5

Brune, J. N. (1968). Seismic moment, seismicity, and rate of slip along major fault zones. *Journal of Geophysical Research*, *73*(2), 777–784. https://doi.org/10.1029/JB073i002p00777

Chen, C.-W., Huang, C.-F., Lin, C.-W., & Kuo, B.-Y. (2017). Hydroacoustic ray theory-based modeling of T wave propagation in the deep ocean basin offshore eastern Taiwan. *Geophysical Research Letters*, *44*(10), 4799–4805. https://doi.org/10.1002/2017GL073516

Chen, Y. J. (1992). Oceanic crustal thickness versus spreading rate. *Geophysical Research Letters*, *19*(8), 753–756. https://doi.org/10.1029/92GL00161

de Groot-Hedlin, C. D. (2005). Estimation of the rupture length and velocity of the great Sumatra earthquake of Dec 26, 2004 using hydroacoustic signals. *Geophysical Research Letters*, *32*(11). https://doi.org/10.1029/2005GL022695

de Groot-Hedlin, C. D., & Orcutt, J. A. (1999). Synthesis of earthquake generated T-waves. *Geophysical Research Letters*, *26*(9), 1227–1230. https://doi.org/10.1029/1999GL900205

Del Pezzo, E., & Giudicepietro, F. (2002). Plane wave fitting method for a plane, small aperture, short period seismic array: A Mathcad program. *Computers & Geosciences*, *28*(1), 59–64. https://doi.org/10.1016/S0098-3004(01)00076-0

de Melo, G., Grevemeyer, I., Lange, D., Metz, D., & Kopp, H. (2024). Relationship between rupture length and magnitude of oceanic transform fault earthquakes [Dataset]. *Zenodo*. https://doi.org/10.5281/zenodo.14237731

de Melo, G. W. S., Mitchell, N. C., & Sokolov, S. Y. (2024). The 2020 Mw 6.6 Vernadsky transform earthquake sequence: Rupture and Coulomb stress changes surrounding an oceanic core complex. *Marine Geophysical Researches*, *45*(4), 28. https://doi.org/10.1007/s11001-024-09558-z

de Melo, G. W. S., Parnell-Turner, R., Dziak, R. P., Smith, D. K., Maia, M., Do Nascimento, A. F., & Royer, J.-Y. (2021). Uppermost mantle velocity beneath the Mid-Atlantic Ridge and transform faults in the equatorial Atlantic ocean. *Bulletin of the Seismological Society of America*, *111*(2), 1067–1079. https://doi.org/10.1785/0120200248

Dziak, R., Bohnenstiehl, D., Matsumoto, H., Fox, C., Smith, D., Tolstoy, M., et al. (2004). P-and t-wave detection thresholds, Pn velocity estimate, and detection of lower mantle and core p-waves on ocean sound-channel hydrophones at the Mid-Atlantic Ridge. *Bulletin of the Seismological Society of America*, *94*(2), 665–677. https://doi.org/10.1785/0120030156

Dziak, R. P., & Fox, C. G. (1999). The January 1998 earthquake swarm at axial volcano, Juan de Fuca ridge: Hydroacoustic evidence of seafloor volcanic activity. *Geophysical Research Letters*, *26*(23), 3429–3432. https://doi.org/10.1029/1999GL002332

Dziewonski, A. M., Chou, T.-A., & Woodhouse, J. H. (1981). Determination of earthquake source parameters from waveform data for studies of global and regional seismicity. *Journal of Geophysical Research*, *86*(B4), 2825–2852. https://doi.org/10.1029/JB086iB04p02825

Ekström, G., Nettles, M., & Dziewon´ski, A. (2012). The global CMT project 2004–2010: Centroid-moment tensors for 13,017 earthquakes. *Physics of the Earth and Planetary Interiors*, *200*, 1–9. https://doi.org/10.1016/j.pepi.2012.04.002

Escartin, J., Hirth, G., & Evans, B. (2001). Strength of slightly serpentinized peridotites: Implications for the tectonics of oceanic lithosphere. *Geology*, *29*(11), 1023–1026. https://doi.org/10.1130/0091-7613(2001)029%3C1023:SOSSPI%3E2.0.CO;2

Fang, H., & Abercrombie, R. E. (2023). Smatstack to enhance noisy teleseismic seismic phases: Validation and application to resolving depths of oceanic transform earthquakes. *Geochemistry, Geophysics, Geosystems*, *24*(11), e2023GC011109. https://doi.org/10.1029/2023GC011109

Frohlich, C., & Wetzel, L. R. (2007). Comparison of seismic moment release rates along different types of plate boundaries. *Geophysical Journal International*, *171*(2), 909–920. https://doi.org/10.1111/j.1365-246X.2007.03550.x

Froment, B., McGuire, J. J., Van Der Hilst, R., Gouedard, P., Roland, E. C., Zhang, H., & Collins, J. A. (2014). Imaging along-strike variations in mechanical properties of the Gofar transform fault, East Pacific Rise. *Journal of Geophysical Research: Solid Earth*, *119*(9), 7175–7194. https://doi.org/10.1002/2014JB011270

Gibbons, S. J. (2022). The hydroacoustic network of the CTBTO international monitoring system: Access and exploitation. *Journal for Peace and Nuclear Disarmament*, *5*(2), 452–468. https://doi.org/10.1080/25751654.2022.2129948

Goldberg, D. E., Koch, P., Melgar, D., Riquelme, S., & Yeck, W. L. (2022). Beyond the teleseism: Introducing regional seismic and geodetic data into routine USGS finite-fault modeling. *Seismological Society of America*, *93*(6), 3308–3323. https://doi.org/10.1785/0220220047

Gregory, E. P., Singh, S. C., Marjanovic, M., & Wang, Z. (2021). Serpentinized peridotite versus thick mafic crust at the Romanche oceanic transform fault. *Geology*, *49*(9), 1132–1136. https://doi.org/10.1130/G49097.1

Grevemeyer, I. (2020). Upper mantle structure beneath the Mid-Atlantic Ridge from regional waveform modeling. *Bulletin of the Seismological Society of America*, *110*(1), 18–25. https://doi.org/10.1785/0120190080

Grevemeyer, I., Ranero, C. R., & Ivandic, M. (2018). Structure of oceanic crust and serpentinization at subduction trenches. *Geosphere*, *14*(2), 395–418. https://doi.org/10.1130/GES01537.1

Guilbert, J., Vergoz, J., Chissele, E., Roueff, A., & Cansi, Y. (2005). Use of hydroacoustic and seismic arrays to observe rupture propagation and source extent of the mw= 9.0 Sumatra earthquake. *Geophysical Research Letters*, *32*(15). https://doi.org/10.1029/2005GL022966

Hicks, S. P., Okuwaki, R., Steinberg, A., Rychert, C. A., Harmon, N., Abercrombie, R. E., et al. (2020). Back-propagating supershear rupture in the 2016 m w 7.1 Romanche transform fault earthquake. *Nature Geoscience*, *13*(9), 647–653. https://doi.org/10.1038/s41561-020-0619-9

Ingale, V. V., Bazin, S., Olive, J.-A., Briais, A., & Royer, J.-Y. (2023). Hydroacoustic study of a seismic swarm in 2016–2017 near the Melville transform fault on the Southwest Indian Ridge. *Bulletin of the Seismological Society of America*, *113*(4), 1523–1541. https://doi.org/10.1785/0120220213

Jamet, G., Guennou, C., Guillon, L., Mazoyer, C., & Royer, J.-Y. (2013). T-Wave generation and propagation: A comparison between data and spectral element modeling. *Journal of the Acoustical Society of America*, *134*(4), 3376–3385. https://doi.org/10.1121/1.4818902

Jordahl, K. (2024). grdread2 [Software]. *MATLAB Central File Exchange*. https://www.mathworks.com/matlabcentral/fileexchange/25683-grdread2

Kanamori, H. (1977). The energy release in great earthquakes. *Journal of Geophysical Research*, *82*(20), 2981–2987. https://doi.org/10.1029/JB082i020p02981

Kanamori, H., & Stewart, G. S. (1976). Mode of the strain release along the Gibbs fracture zone, Mid-Atlantic Ridge. *Physics of the Earth and Planetary Interiors*, *11*(4), 312–332. https://doi.org/10.1016/0031-9201(76)90018-2

Kohli, A., Wolfson-Schwehr, M., Prigent, C., & Warren, J. M. (2021). Oceanic transform fault seismicity and slip mode influenced by seawater infiltration. *Nature Geoscience*, *14*(8), 606–611. https://doi.org/10.1038/s41561-021-00778-1

Konstantinou, K. I., Papadopoulos, G. A., Fokaefs, A., & Orphanogiannaki, K. (2005). Empirical relationships between aftershock area dimensions and magnitude for earthquakes in the Mediterranean Sea region. *Tectonophysics*, *403*(1–4), 95–115. https://doi.org/10.1016/j.tecto.2005.04.001

Leptokaropoulos, K., Rychert, C. A., Harmon, N., Schlaphorst, D., Grevemeyer, I., Kendall, J.-M., & Singh, S. C. (2023). Broad fault zones enable deep fluid transport and limit earthquake magnitudes. *Nature Communications*, *14*(1), 5748. https://doi.org/10.1038/s41467-023-41403-6

Maggi, A., Jackson, J., Mckenzie, D., & Priestley, K. (2000). Earthquake focal depths, effective elastic thickness, and the strength of the continental lithosphere. *Geology*, *28*(6), 495–498. https://doi.org/10.1130/0091-7613(2000)28%3C495:EFDEET%3E2.0.CO;2

Mai, P. M., & Beroza, G. C. (2000). Source scaling properties from finite-fault-rupture models. *Bulletin of the Seismological Society of America*, *90*(3), 604–615. https://doi.org/10.1785/0119990126

Maia, M. (2019). Topographic and morphologic evidences of deformation at oceanic transform faults: Far-field and local-field stresses. In *Transform Plate Boundaries and Fracture Zones* (pp. 61–87). Elsevier. https://doi.org/10.1016/B978-0-12-812064-4.00003-7

Maia, M., Sichel, S., Briais, A., Brunelli, D., Ligi, M., Ferreira, N., et al. (2016). Extreme mantle uplift and exhumation along a transpressive transform fault. *Nature Geoscience*, *9*(8), 619–623. https://doi.org/10.1038/ngeo2759

McGuire, J. J., Collins, J. A., Gouedard, P., Roland, E., Lizarralde, D., Boettcher, M. S., et al. (2012). Variations in earthquake rupture properties along the Gofar transform fault, East Pacific Rise. *Nature Geoscience*, *5*(5), 336–341. https://doi.org/10.1038/ngeo1454

McGuire, J. J., Ihmle, P. F., & Jordan, T. H. (1996). Time-domain observations of a slow precursor to the 1994 Romanche transform earthquake. *Science*, *274*(5284), 82–85. https://doi.org/10.1126/science.274.5284.82

Metz, D., Watts, A., Grevemeyer, I., & Rodgers, M. (2018). Tracking submarine volcanic activity at monowai: Constraints from long-range hydroacoustic measurements. *Journal of Geophysical Research: Solid Earth*, *123*(9), 7877–7895. https://doi.org/10.1029/2018JB015888

Metz, D., Watts, A. B., Grevemeyer, I., Rodgers, M., & Paulatto, M. (2016). Ultra-long-range hydroacoustic observations of submarine volcanic activity at Monowai, Kermadec arc. *Geophysical Research Letters*, *43*(4), 1529–1536. https://doi.org/10.1002/2015GL067259

Ogden, C., & Bastow, I. (2022). The crustal structure of the Anatolian plate from receiver functions and implications for the uplift of the central and eastern Anatolian plateaus. *Geophysical Journal International*, *229*(2), 1041–1062. https://doi.org/10.1093/gji/ggab513

Okal, E. A. (2008). The generation of t waves by earthquakes. *Advances in Geophysics*, *49*, 1–65. https://doi.org/10.1016/S0065-2687(07)49001-X

Okal, E. A., & Talandier, J. (1986). T-Wave duration, magnitudes, and seismic moment of an earthquake: Application to Tsunami warning. *Journal of Physics of the Earth*, *34*(1), 19–42. https://doi.org/10.4294/jpe1952.34.19

Palacios, R. (2024). deg2utm [Software]. *MATLAB Central File Exchange*. https://www.mathworks.com/matlabcentral/fileexchange/10915-deg2utm

Parnell-Turner, R., Smith, D., & Dziak, R. (2022). Hydroacoustic monitoring of seafloor spreading and transform faulting in the equatorial Atlantic Ocean. *Journal of Geophysical Research: Solid Earth*, *127*(7), e2022JB024008. https://doi.org/10.1029/2022JB024008

Prigent, C., Warren, J., Kohli, A., & Teyssier, C. (2020). Fracture-mediated deep seawater flow and mantle hydration on oceanic transform faults. *Earth and Planetary Science Letters*, *532*, 115–988. https://doi.org/10.1016/j.epsl.2019.115988

Pro, C., Buforn, E., & Udías, A. (2007). Rupture length and velocity for earthquakes in the Mid-Atlantic Ridge from directivity effect in body and surface waves. *Tectonophysics*, *433*(1–4), 65–79. https://doi.org/10.1016/j.tecto.2006.12.011

Ren, Y., Geersen, J., & Grevemeyer, I. (2021). Global compilation of shipborne bathymetric data from oceanic transform fault systems at ultraslow-to fast-spreading ridges [Dataset]. In *Geophysical Research Letters*. Zenodo. https://doi.org/10.5281/zenodo.4774185

Ren, Y., Geersen, J., & Grevemeyer, I. (2022). Impact of spreading rate and age-offset on oceanic transform fault morphology. *Geophysical Research Letters*, *49*(2), e2021GL096170. https://doi.org/10.1029/2021GL096170

Rodríguez-Pérez, Q., & Ottemöller, L. (2014). Source study of the Jan Mayen transform fault strike-slip earthquakes. *Tectonophysics*, *628*, 71–84. https://doi.org/10.1016/j.tecto.2014.04.035

Romanowicz, B., & Ruff, L. (2002). On moment-length scaling of large strike slip earthquakes and the strength of faults. *Geophysical Research Letters*, *29*(12), 45–51. https://doi.org/10.1029/2001GL014479

Ross, Z. E., Idini, B., Jia, Z., Stephenson, O. L., Zhong, M., Wang, X., et al. (2019). Hierarchical interlocked orthogonal faulting in the 2019 Ridgecrest earthquake sequence. *Science*, *366*(6463), 346–351. https://doi.org/10.1126/science.aaz0109

Ryan, W. B. F., Carbotte, S. M., Coplan, J. O., O'Hara, S., Melkonian, A., Arko, R., et al. (2009). Global multi-resolution topography synthesis. *Geochemistry, Geophysics, Geosystems*, *10*(3), Q03014. https://doi.org/10.1029/2008GC002332

Sallares, V., & Ranero, C. R. (2019). Upper-plate rigidity determines depth-varying rupture behaviour of megathrust earthquakes. *Nature*, *576*(7785), 96–101. https://doi.org/10.1038/s41586-019-1784-0

Sautter, B., Escartin, J., Petersen, S., Gaina, C., Granot, R., & Pubellier, M. (2024). Mapridges: Global database of mid-oceanic ridges segments and transform faults. *SEANOE*. https://doi.org/10.17882/99981

Scholz, C. (1988). The brittle-plastic transition and the depth of seismic faulting. *Geologische Rundschau*, *77*(1), 319–328. https://doi.org/10.1007/BF01848693

Searle, R., & Escartin, J. (2013). The rheology and morphology of oceanic lithosphere and mid-ocean ridges. In *Mid Ocean Ridges: Hydrothermal Interactions Between the Lithosphere and the Oceans* (Vol. 148, pp. 63–93). American Geophysical Union. https://doi.org/10.1029/148GM03

Searle, R., Thomas, M., & Jones, E. (1994). Morphology and tectonics of the Romanche transform and its environs. *Marine Geophysical Researches*, *16*(6), 427–453. https://doi.org/10.1007/BF01270518

Shearer, P., & Bürgmann, R. (2010). Lessons learned from the 2004 Sumatra-Andaman megathrust rupture. *Annual Review of Earth and Planetary Sciences*, *38*(1), 103–131. https://doi.org/10.1146/annurev-earth-040809-152537

Shearer, P. M. (2019). *Introduction to seismology*. Cambridge University Press. https://doi.org/10.1017/9781316877111

Smith, D. K., Escartin, J., Cannat, M., Tolstoy, M., Fox, C. G., Bohnenstiehl, D. R., & Bazin, S. (2003). Spatial and temporal distribution of seismicity along the northern Mid-Atlantic Ridge (15–35 n). *Journal of Geophysical Research*, *108*(B3). https://doi.org/10.1029/2002JB001964

Smith-Konter, B. R., Sandwell, D. T., & Shearer, P. (2011). Locking depths estimated from geodesy and seismology along the San Andreas Fault system: Implications for seismic moment release. *Journal of Geophysical Research*, *116*(B6), B06401. https://doi.org/10.1029/2010JB008117

Talandier, J., & Okal, E. A. (1998). On the mechanism of conversion of seismic waves to and from T waves in the vicinity of island shores. *Bulletin of the Seismological Society of America*, *88*(2), 621–632. https://doi.org/10.1785/BSSA0880020621

The MathWorks Inc. (2020). MATLAB version: 9.8 (R2020a) [Software]. The MathWorks Inc. https://www.mathworks.com

Tolstoy, I., & Ewing, M. (1950). The t phase of shallow-focus earthquakes. *Bulletin of the Seismological Society of America*, *40*(1), 25–51. https://doi.org/10.1785/BSSA0400010025

Tolstoy, M., & Bohnenstiehl, D. R. (2005). Hydroacoustic constraints on the rupture duration, length, and speed of the great Sumatra-Andaman earthquake. *Seismological Research Letters*, *76*(4), 419–425. https://doi.org/10.1785/gssrl.76.4.419

Vallee, M., & Douet, V. (2016). A new database of source time functions (STFs) extracted from the SCARDEC method. *Physics of the Earth and Planetary Interiors*, *257*, 149–157. https://doi.org/10.1016/j.pepi.2016.05.012

Various Institutions. (1965). International Miscellaneous stations [Dataset]. *International Federation of Digital Seismograph Networks*. https://doi.org/10.7914/vefq-vh75

Vera, F., Tilmann, F., & Saul, J. (2024). A decade of short-period earthquake rupture histories from multi-array back-projection. *Journal of Geophysical Research: Solid Earth*, *129*(2), e2023JB027260. https://doi.org/10.1029/2023JB027260

Wells, D. L., & Coppersmith, K. J. (1994). New empirical relationships among magnitude, rupture length, rupture width, rupture area, and surface displacement. *Bulletin of the Seismological Society of America*, *84*(4), 974–1002. https://doi.org/10.1785/BSSA0840040974

Wessel, P., Luis, J. F., Uieda, L., Scharroo, R., Wobbe, F., Smith, W. H. F., & Tian, D. (2019). The generic mapping Tools version 6. *Geochemistry, Geophysics, Geosystems*, *20*(11), 5556–5564. https://doi.org/10.1029/2019GC008515

Wilson, J. T. (1965). A new class of faults and their bearing on continental drift. *Nature*, *207*(4995), 343–347. https://doi.org/10.1038/207343a0

Wolfson-Schwehr, M., & Boettcher, M. S. (2019). Global characteristics of oceanic transform fault structure and seismicity. In *Transform Plate Boundaries and Fracture Zones* (pp. 21–59). Elsevier. https://doi.org/10.1016/B978-0-12-812064-4.00002-5

Yang, Y., & Forsyth, D. W. (2003). Improving epicentral and magnitude estimation of earthquakes from T-phases by considering the excitation function. *Bulletin of the Seismological Society of America*, *93*(5), 2106–2122. https://doi.org/10.1785/0120020215

Yang, Z., Zhao, D., Cheng, B., & Dong, Y. (2022). Structural control on the 2019 Ridgecrest earthquake from local seismic tomography. *Physics of the Earth and Planetary Interiors*, *324*, 106–853. https://doi.org/10.1016/j.pepi.2022.106853

References From the Supporting Information

Blackman, D. K., Karson, J. A., Kelley, D. S., Cann, J. R., Früh-Green, G. L., Gee, J. S., et al. (2002). Geology of the Atlantis Massif (Mid-Atlantic Ridge, 30 N): Implications for the evolution of an ultramafic oceanic core complex. *Marine Geophysical Researches*, *23*(5/6), 443–469. https://doi.org/10.1023/B:MARI.0000018232.14085.75

Bohnenstiehl, D. R., Tolstoy, M., Smith, D. K., Fox, C. G., & Dziak, R. P. (2003). Time-clustering behavior of spreading-center seismicity between 15 and 35 N on the Mid-Atlantic Ridge: Observations from hydroacoustic monitoring. *Physics of the Earth and Planetary Interiors*, *138*(2), 147–161. https://doi.org/10.1016/S0031-9201(03)00113-4

Buehler, J. S., & Shearer, P. M. (2014). Anisotropy and Vp/Vs in the uppermost mantle beneath the western United States from joint analysis of Pn and Sn phases. *Journal of Geophysical Research: Solid Earth*, *119*(2), 1200–1219. https://doi.org/10.1002/2013JB010559

Campos, T. F. C., Neto, J. V., Amorim, V. A., Hartmann, L. A., & Petta, R. A. (2003). Modificações metassomáticas das rochas milonitizadas do complexo ultramáfico do Arquipélago de São Pedro e São Paulo, Atlântico Equatorial. *Geochimica Brasiliensis*, *17*(2). https://geobrasiliensis.org.br/geobrasiliensis/article/view/201

Campos, T. F., Sichel, S. E., Maia, M., Brunelli, D., Motoki, K., Magini, C., & de Melo, G. (2022). The singular St. Peter and St. Paul Archipelago, equatorial Atlantic, Brazil. In *Meso-cenozoic Brazilian offshore Magmatism* (pp. 121–165). Academic Press. https://doi.org/10.1016/B978-0-12-823988-9.00003-4

Christensen, N. I. (1996). Poisson's ratio and crustal seismology. *Journal of Geophysical Research*, *101*(B2), 3139–3156. https://doi.org/10.1029/95JB03446

Dziak, R. P. (2001). Empirical relationship of T-wave energy and fault parameters of northeast Pacific Ocean earthquakes. *Geophysical Research Letters*, *28*(13), 2537–2540. https://doi.org/10.1029/2001GL012939

Erbe, C. (2011). Underwater acoustics: Noise and the effects on marine mammals. In *A Pocket Handbook* (3rd ed., p. 23p). JASCO Applied Science.

Grevemeyer, I., Reston, T. J., & Moeller, S. (2013). Microseismicity of the mid-Atlantic Ridge at 7° S–8° 15′ S and at the Logatchev Massif oceanic core complex at 14° 40′ N–14° 50′ N. *Geochemistry, Geophysics, Geosystems*, *14*(9), 3532–3554. https://doi.org/10.1002/ggge.20197

Grevemeyer, I., Hayman, N. W., Peirce, C., Schwardt, M., Van Avendonk, H. J., Dannowski, A., & Papenberg, C. (2018). Episodic magmatism and serpentinized mantle exhumation at an ultraslow-spreading centre. *Nature Geoscience*, *11*(6), 444–448. https://doi.org/10.1038/s41561-018-0124-6

Hekinian, R., Juteau, T., Gracia, E., Sichler, B., Sichel, S., Udintsev, G., et al. (2000). Submersible observations of equatorial Atlantic mantle: The St. Paul Fracture zone region. *Marine Geophysical Researches*, *21*(6), 529–560. https://doi.org/10.1023/A:1004819701870

Ito, A., Sugioka, H., Suetsugu, D., Shiobara, H., Kanazawa, T., & Fukao, Y. (2012). Detection of small earthquakes along the Pacific-Antarctic Ridge from T-waves recorded by abyssal ocean-bottom observatories. *Marine Geophysical Researches*, *33*(3), 229–238. https://doi.org/10.1007/s11001-012-9158-0

Ji, C., Wald, D. J., & Helmberger, D. V. (2002). Source description of the 1999 Hector Mine, California, earthquake, part I: Wavelet domain inversion theory and resolution analysis. *Bulletin of the Seismological Society of America*, *92*(4), 1192–1207. https://doi.org/10.1785/0120000916

Ji, S., Li, A., Wang, Q., Long, C., Wang, H., Marcotte, D., & Salisbury, M. (2013). Seismic velocities, anisotropy, and shear-wave splitting of antigorite serpentinites and tectonic implications for subduction zones. *Journal of Geophysical Research: Solid Earth*, *118*(3), 1015–1037. https://doi.org/10.1002/jgrb.50110

Metz, D., Nielson, P., Zampolli, M., & Haralabus, G. (2021). Remote detection of hydroacoustic signals potentially associated with the sinking of SS El Faro using CTBT IMS hydrophone data. *CTBT Science and Technology Conference*, *2021*, P1.3–331.

Li, Z., Wiens, D. A., Shen, W., & Shillington, D. J. (2024). Along-strike variations of Alaska subduction zone structure and hydration determined from amphibious seismic data. *Journal of Geophysical Research: Solid Earth*, *129*(3), e2023JB027800. https://doi.org/10.1029/2023JB027800

Liu, T., Gong, J., Fan, W., & Lin, G. (2023). In-situ Vp/Vs reveals fault-zone material variation at the westernmost Gofar Transform Fault, East Pacific Rise. *Journal of Geophysical Research: Solid Earth*, *128*(3), e2022JB025310. https://doi.org/10.1029/2022JB025310

McGuire, J. J. (2008). Seismic cycles and earthquake predictability on East Pacific Rise transform faults. *Bulletin of the Seismological Society of America*, *98*(3), 1067–1084. https://doi.org/10.1785/0120070154

Okal, E. A. (2008). The generation of T waves by earthquakes. *Advances in Geophysics*, *49*, 1–65. https://doi.org/10.1016/j.pepi.2009.03.002

Pan, J., Antolik, M., & Dziewonski, A. M. (2002). Locations of mid-oceanic earthquakes constrained by seafloor bathymetry. *Journal of Geophysical Research*, *107*(B11), EPM–8. https://doi.org/10.1029/2001JB001588

Pan, J., & Dziewonski, A. M. (2005). Comparison of mid-oceanic earthquake epicentral differences of travel time, centroid locations, and those determined by autonomous underwater hydrophone arrays. *Journal of Geophysical Research*, *110*(B7). https://doi.org/10.1029/2003JB002785

Parsons, B., & Sclater, J. G. (1977). An analysis of the variation of ocean floor bathymetry and heat flow with age. *Journal of Geophysical Research*, *82*(5), 803–827. https://doi.org/10.1029/JB082i005p00803

Romanowicz, B., Cara, M., Fel, J. F., & Rouland, D. (1984). Geoscope: A French initiative in long-period three-component global seismic networks. *Eos, Transactions American Geophysical Union*, *65*(42), 753. https://doi.org/10.1029/EO065i042p00753-01

Searle, R. (2013). *Mid-ocean ridges*. Cambridge University Press. https://doi.org/10.1017/CBO9781139084260

Seton, M., Müller, R. D., Zahirovic, S., Williams, S., Wright, N. M., Cannon, J., et al. (2020). A global data set of present-day oceanic crustal age and seafloor spreading parameters. *Geochemistry, Geophysics, Geosystems*, *21*(10), e2020GC009214. https://doi.org/10.1029/2020GC009214

Toda, S., Stein, R. S., Sevilgen, V., & Lin, J. (2011). Coulomb 3.3 graphic-rich deformation and stress-change software for earthquake, tectonic, and volcano research and teaching—User guide. *US Geological Survey open-file report*, *1060*(2011), 63. https://pubs.usgs.gov/of/2011/1060/

Tozer, B., Sandwell, D. T., Smith, W. H., Olson, C., Beale, J. R., & Wessel, P. (2019). Global bathymetry and topography at 15 arc sec: SRTM15+. *Earth and Space Science*, *6*(10), 1847–1864. https://doi.org/10.1029/2019ea000658

Turcotte, D. L., & Schubert, G. (2002). *Geodynamics*. Cambridge University Press. https://doi.org/10.1017/CBO9780511843877

U.S. Geological Survey. (2024). Earthquake lists, maps, and Statistics. Retrieved from https://earthquake.usgs.gov/earthquakes/search/

Wang, Z., Singh, S. C., Prigent, C., Gregory, E. P., & Marjanović, M. (2022). Deep hydration and lithospheric thinning at oceanic transform plate boundaries. *Nature Geoscience*, *15*(9), 741–746. https://doi.org/10.1038/s41561-022-01003-3